Subdiffusive movement of chromosomal loci in bacteria explained by DNA bridging

Srikanth Subramanian ● and Seán M. Murray ●[*]

Max Planck Institute for Terrestrial Microbiology, Marburg 35043, Germany

Chromosomal loci in bacterial cells show a robust subdiffusive scaling of the mean square displacement, $\mathrm{MSD}(\tau) \sim \tau^\alpha$, with $\alpha < 0.5$. On the other hand, recent experiments have also shown that DNA-bridging nucleoid associated proteins (NAPs) play an important role in chromosome organization and compaction. Here, using polymer simulations we investigate the role of DNA bridging in determining the dynamics of chromosomal loci. We find that bridging compacts the polymer and reproduces the subdiffusive elastic dynamics of monomers at timescales shorter than the bridge lifetime. Consistent with this prediction, we measure a higher exponent in a NAP mutant compared to the wild type. Furthermore, bridging can reproduce the rare but ubiquitous rapid movements of chromosomal loci that have been observed in experiments. In our model the scaling exponent defines a relationship between the abundance of bridges and their lifetime. Using this and the observed mobility of chromosomal loci, we predict a lower bound on the average bridge lifetime of around five seconds.

I. INTRODUCTION

The diffusive dynamics of chromosomal loci have been characterised *in vivo* in several bacterial species by measuring the scaling exponent α of the mean square displacement $\mathrm{MSD}(\tau) = \langle (\boldsymbol{r}(t + \tau) - \boldsymbol{r}(t))^2 \rangle \sim \tau^\alpha$. However, while polymer theory predicts a subdiffusive scaling exponent of $\alpha = 2\nu/(2\nu + 1) \approx 0.54$ for a self-avoiding Rouse polymer ($\nu \approx 0.588$) [1,2], the values measured for chromosomal loci are consistently less than this across different species, strains, and conditions [3–8]. Fractional Brownian motion (fBm) due to the viscoelastic nature of the cytoplasm has been proposed as a possible explanation [3,9]. However, this model cannot reproduce the rare but ubiquitous rapid chromosomal movements (RCMs) made by loci [10] and its predictions are inconsistent with a recent study in which compression of the cell was found to only affect the exponent of chromosomal loci and not cytosolic particles [6]. Other mechanisms are therefore required to explain the observed low subdiffusive exponent.

Nucleoid associated proteins (NAPs) are DNA-binding proteins that condense and organize the bacterial nucleoid through bridging, bending, or stiffening the DNA [11–13]. Recent work using high-throughput chromosome conformation capture (HiC) has investigated how different NAPs affect the contact probability between chromosomal loci [14]. The obtained two-point contact probabilities have then been used in polymer models to specify an attractive potential between monomers and make predictions about the spatial organization of the chromosome within the cell and the dynamics of individual loci [15–20].

A different approach is to explicitly examine the effect of bridging on the polymer. The earliest work on this is in the context of the entangled and unentangled reversible networks and gels formed by associative polymers and particularly in how bridging affects the relaxation dynamics of the polymer network [21–24]. More recently, and at the other extreme of high bridge density, computational models have explored how the resulting globular state can explain the organization of eukaryotic chromatin [25–32]. Connected to the present study, dynamic bridging was also shown to decrease the MSD scaling exponent of single monomers in line with measurements of chromosomal loci in bacteria and yeast [33]. However, a systematic study of how the exponent depends on the number of bridges and their lifetime has yet to be performed. Furthermore, it is not clear whether bridging can also explain the presence of RCMs [10].

Here, in the absence of a dynamical theory, we use polymer simulations to investigate how DNA bridging affects the dynamics of the bacterial chromosome. We confirm that bridging can reduce the scaling exponent of individual monomers below the classic prediction of polymer theory and characterize the dependence on both the number of bridges and their lifetime. Consistent with these results, we show in *E. coli* that deleting the bridging protein H-NS results in an increase in the scaling exponent compared to wild type. We also find that bridging produces monomer dynamics that display the same RCMs as have been observed experimentally. Finally, we use the experimentally observed mobility of loci to fix an internal timescale in our simulations and thereby predict a lower bound for the average bridge lifetime.

II. POLYMER SIMULATIONS

We simulate a self-avoiding linear polymer using the Bond Fluctuation method (BFM) [34,35]. This lattice

---

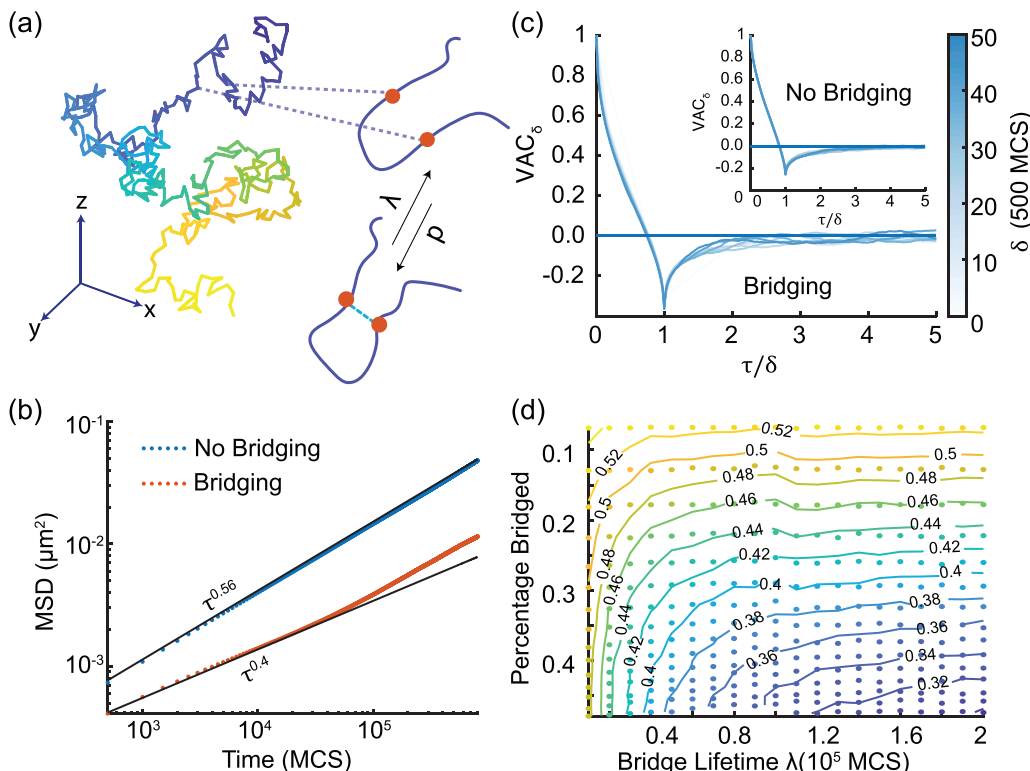*sean.murray@synmikro.mpi-marburg.mpg.de

FIG. 1. (a) The simulated polymer. Bridges form between spatially proximal monomers with a probability p and have a mean lifetime λ. (b) Ensemble-averaged MSD curves with (orange) and without bridging (blue). Bridging parameters: $p = 1.5 \times 10^{-3}$, $\lambda = 4 \times 10^{4}$ MCS. (c) Phase diagram from Fig. 9(a) with μ remapped to the percentage of monomers bridged. Contours indicate interpolated curves of the given exponent. (d) Velocity auto-correlation function (VAC) is negative at short lags and collapses for different windows of τ/δ, indicative of a subdiffusive process.

polymer model is ergodic, allows a large set of bond angles, and reproduces Rouse polymer dynamics. Each monomer is represented by a cube (voxel) of the lattice and exclusively occupies the corresponding 8 lattice vertices. Neighboring monomers are connected by one of 108 allowed bond vectors with lengths 2, $\sqrt{5}$, $\sqrt{6}$, 3, or $\sqrt{10}$. We use the open source software LeMonADE [36] and modified it to add bridging functionality. The basic (without bridging) simulation is specified by the number of monomers N and the lattice dimension L [see Appendix A].

A. Excluded volume of the polymer

Since each monomer is represented by a cube exclusively occupying eight vertices, the excluded volume of each monomer is the set of $3 \times 3 \times 3 = 27$ cubes around the monomer. Note however that the excluded volume of different monomers can partially overlap. The excluded volume V of the entire polymer is therefore the union of the excluded volume of the individual monomers. We find that with a length of 400 monomers, the polymer occupies a total of approximately 8678 lattice sites or an average of 21.69 unique lattice sites per monomer.

We fix the lattice dimension L by using this volume measure to match the volume density of chromosome in the cell

($\sim 1\%$)

$$\rho = \frac{V}{L^3} = \frac{8678}{L^3} = 1\%. \tag{1}$$

This fixes the dimension of the lattice at $L = 95$ lattice units.

In order to compare the simulated MSD data with experiments at short time lags we require sufficient spatial resolution at ~ 0.004 μm^2, the MSD of chromosomal loci at 1 s lag [3,5]. We therefore fix the lattice spacing to be $h = 0.0056$ μm. The number of base pairs corresponding to a monomer in our simulations is given by

$$\frac{\text{base pair}}{\text{monomer}} = \frac{L_g}{V_c} \frac{V_b}{N}, \tag{2}$$

where $V_c \approx 0.88$ μm^3 is the volume of the cell, $L_g = 4.5$ Mbp the length of *E. coli* genome, and $V_b = L^3 h^3$ the volume of the box. Hence, we simulate an 800 kb segment (approximately the size of a macrodomain) of the chromosome with each monomer representing a 2 kb segment of chromosome. We use periodic boundary conditions in our simulations.

B. Bridging

We implement bridging following the approach of Bohn and Heermann [33], where we select two monomers on the polymer at random and check its colocalize at a distance less
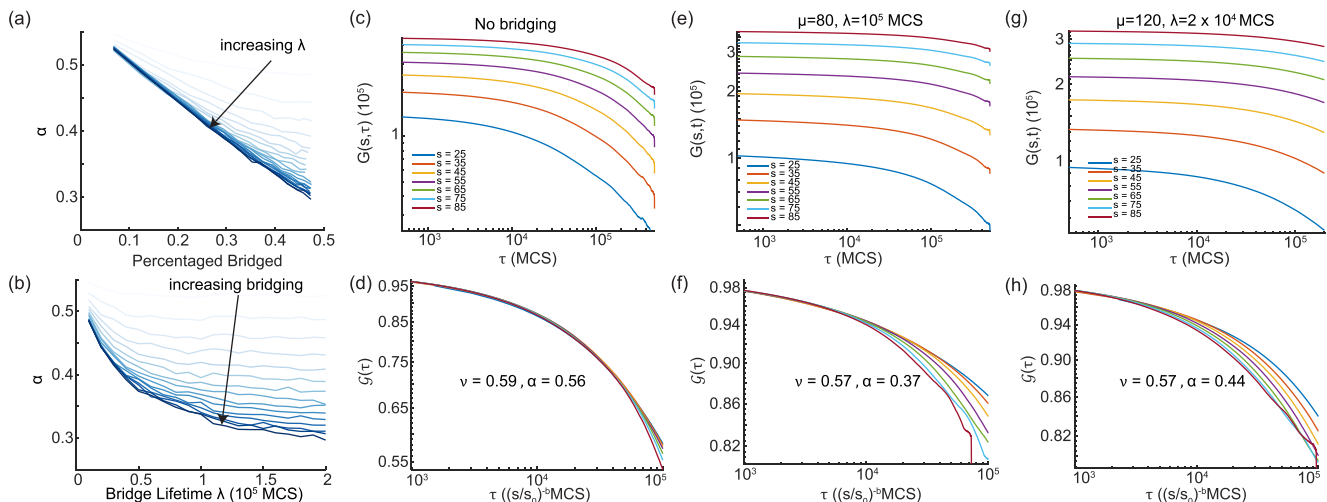
FIG. 2. (a) The scaling exponent α is plotted as a function of percentage bridged for different bridge lifetimes (color). (b) α as function of bridge lifetime for different values of μ (color). Note that the curves come closer together because of the relationship in Fig. S1(e). (c), (e), (g) The two-point correlation function $G(s, \tau)$ is calculated from our simulations for different parameters. (d), (f), (h) Shows the collapse of curves in (c), (e), (g) upon rescaling time by $\tau \to s^{-b}\tau$. In the absence of bridging (d) we found that a slightly different exponent $b = 1.9$ fits better than the expected $b = 2.1$. In (f), (g) the calculated values of $b = 3.03$, $b = 2.59$ resulted in good collapse. In (d), (f), (h) $s_0 = 45$ is a reference distance for plotting.

than three lattice units. A bridge is formed with a probability p that lasts an average bridge lifetime λ. While bridged, monomers can still move on the lattice subject to maintaining a bridge length less than three lattice units. Each monomer can only form one bridge at a time [Fig. 1(a)].

C. Bridging leads to loci subdiffusion

We confirmed that bridging reduces the scaling exponent of a single monomer [Fig. 1(b)], as has been previously shown in study of eukaryotic chromatin [33]. At a level of bridging that results in 28% of monomers bridged, the exponent decreased from $\alpha \approx 0.56$ (close to the scaling theory prediction of 0.54) to $\alpha \approx 0.4$, a value in line with experimental measurements [3].

To examine the dynamics further, we measured the velocity auto-correlation (VAC) function,

$$\text{VAC}_\delta(\tau) = \frac{1}{\delta^2}\langle(\boldsymbol{r}(\tau + \delta) - \boldsymbol{r}(\tau)) \cdot (\boldsymbol{r}(\delta) - \boldsymbol{r}(0))\rangle,$$

of a monomer with the velocity measured over time points δ MCS apart. Bridging does not change the nature of the VAC, which remains negative at short time lags with the lowest value at lag equal to δ [Fig. 1(c)]. This is indicative of elastic or sub-diffusive dynamics and is consistent with experimental measurements of chromosomal loci [3,9,37].

To systematically examine the effect of bridging, we varied the bridging probability p and bridge lifetime λ over a range of values. We found that the number of bridged monomers depends only on the product $\mu = p\lambda$ as would be the case for a simple reversible process. As a dynamical measure, the scaling exponent α depends on both μ and λ; the more bridges and the longer their lifetime, the greater the reduction of the scaling exponent. As the number of bridges is the more important quantity, we remapped the phase diagram in terms it rather than the parameter μ [Fig. 1(d)]. This makes it clear that,

for sufficiently long bridge lifetimes, an increase (decrease) in the number of bridges formed is concomitant with a decrease (increase) of the scaling exponent. The dependence of α on the number of bridges also become linear for longer lifetimes, at least in the measured range [Fig. 2(a)]. See Appendix B for a detailed discussion on equilibrium properties.

D. Two-point correlation function

A scaling argument was recently proposed relating the dynamic scaling exponent α, the fractal dimension $1/\nu$ and an exponent $b = 2\nu/\alpha$ that specifies a time rescaling and resultant collapse of the two-point correlation function into a distance-independent form [38]

$$G(s, \tau) \equiv \langle[R_n(t + \tau) - R_m(t + \tau)][R_n(t) - R_m(t)]\rangle_{|n-m|=s}, \tag{3}$$

namely

$$G(s, \tau) = As^{2\nu}\mathcal{G}(s^{-b}\tau), \tag{4}$$

where the prefactor A is defined by $G(s, 0) = r(s) = As^{2\nu}$. Thus, $\mathcal{G}(\tau s^{-b})$ is the normalized two-point correlation and the form of its argument indicates that a transformation $\tau \to s^{-b}\tau$ collapses it onto a single curve for all s.

To test this, we used the measured values ν and α at a different bridging parameters and examined the collapse of correlation function at the predicted value of b. In the absence of bridging, we found $\nu = 0.59$, $\alpha = 0.56$, and hence, $b = 2.1$. However, we found that the curves collapse for a slightly lower exponent of $b = 1.9$ [Fig. 2(d)], likely due to the self-avoidance of the polymer. In the presence of bridging, predicted exponent b resulted in a very clear collapse of the curves [Figs. 2(f) and 2(h)] but only at short lags. This could be explained by the fact that we do not have a single dynamic exponent α—the MSD curve transitions at a lag on the order of the bridge lifetime to the standard exponent of ≈ 0.54. While self-avoidance and lack of a single dynamical exponent

[see Fig. 1(b) and below], leads to some discrepancies, overall the results of our simulation are in broad agreement with this proposal [Figs. 2(c)–2(h)].

III. LOCI TRACKING EXPERIMENTS

As discussed above, some nucleoid associated proteins (NAPs) can form bridges between genomically distant DNA. Therefore, our model predicts that the deletion of a bridging NAP should increase the scaling exponent. To test this we measured the MSD scaling exponent of a chromosomal locus in a strain lacking the NAP H-NS. We choose this protein as its deletion produces a very mild phenotype [14] (thus reducing the likelihood of indirect effects), and it bridges rather than bends DNA like other NAPs such as HU, FIS, and IHF. MukBEF can also bridge DNA but also likely extrudes DNA loops [13]. Following previous work [5], we used fluorescence microscopy and the GFP-ParB/*parS* labeling system [39] to track the *ori* locus of *E. coli* on short timescales.

A. Strains

The *parS*/P1 site from *E. coli* strain RM29 obtained from [40] (originally from [39]) was transduced near the *ori* region into MG1655 WT and ΔHNS strains, the latter obtained from the Keio collection of the Sourjik laboratory (MPI Terrestrial Microbiology). GFP-ParB was expressed from the plasmid pALA2705 with no IPTG induction [39,41,42]. The strains were grown overnight at 30 °C in LB medium with appropriate antibiotics (100 μg/mL ampicillin). The overnight culture was diluted into media made of M9-Glucose-Casamino acids (as in [5]) and grown to an optical density of 0.1–0.2.

We chose the P1 labeling system in order to compare our results with previous studies [3,5,10,43]. We note that while some differences in the dynamics of the *ter* locus between the ParB labeling systems, we use (P1), compared to that of pMT1 have been observed, no substantial differences have been reported for the *ori* locus [8,41,42,44]. This agrees with experiments in our laboratory studying origin positioning and segregation across many thousands of cell cycles.

B. Microscopy

1 μL of the sample was placed on 1.5% agraose pads (made of same media as the day culture) and imaged under a Nikon Ti microscope with a 60×/1.4 NA oil objective. The strains were imaged at a constant 30 °C. Images were captured on a Hamamatsu CCD camera using NIS-Elements software. Movies were 450 frames long, with 0.1s interval and an exposure time of 100 ms [Fig. 3(a)].
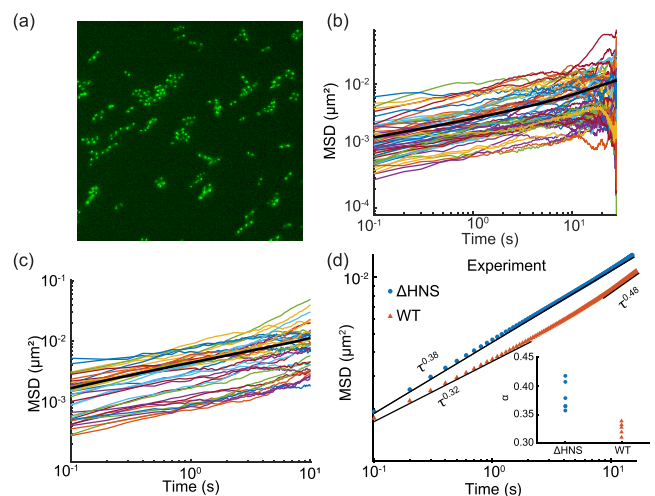

FIG. 3. (a) Snapshot of microscopy experiment of GFP-ParB/**parS** labeled *ori* loci in *E. coli*. (b) Sample MSD curves of individual foci obtained from WT strain (set 1). (c) Sample MSD curves of mutant ΔHNS (set 1). Ensemble averaged MSD is represented by the black lines (b), (c). (d) Ensemble-averaged MSD curves from experiments of wild-type *E. coli* and a strain lacking the NAP H-NS (see also Fig. 6). MSD curves are fitted up to a 2 s delay (black lines). ΔH-NS: $\alpha = 0.38$ 18089 tracks, WT: $\alpha = 0.32$ 6717 tracks. Inset: Exponent α from individual replicates (see Table I).

C. Analysis

We follow the procedure and analysis in [5]. Briefly, foci positions were located via twodimensional fitting of a Gaussian function to the intensity distributions of individual loci. The ensemble averaged MSD was calculated from pooled trajectories using Eq. (A1). The scaling exponent α was calculated for ensemble averaged MSD curves by fitting a power law up to 2 s delays [Figs. 3(b) and 3(c)].

The code of Javer *et al.* was used to track the foci, and are available at [45]. Custom MATLAB scripts were written to analyze the data.

D. Scaling exponents of WT and ΔH-NS

The ensemble-averaged MSD of both the wild type and the ΔH-NS strain are shown in Fig. 3(d). We found that the scaling exponent α for the ΔH-NS ($\alpha \sim 0.38$) is greater than that of the wild type $\alpha \sim 0.32$, consistent with a decrease in the number of DNA bridges. While, we observe some variability in the exact value of the exponents between biological replicates (see inset), the exponent of ΔH-NS is consistently higher than the wild type. This result was not attributable to differences in the signal intensity between the strains

TABLE I. Table of scaling exponents α observed in experiments from different sessions.

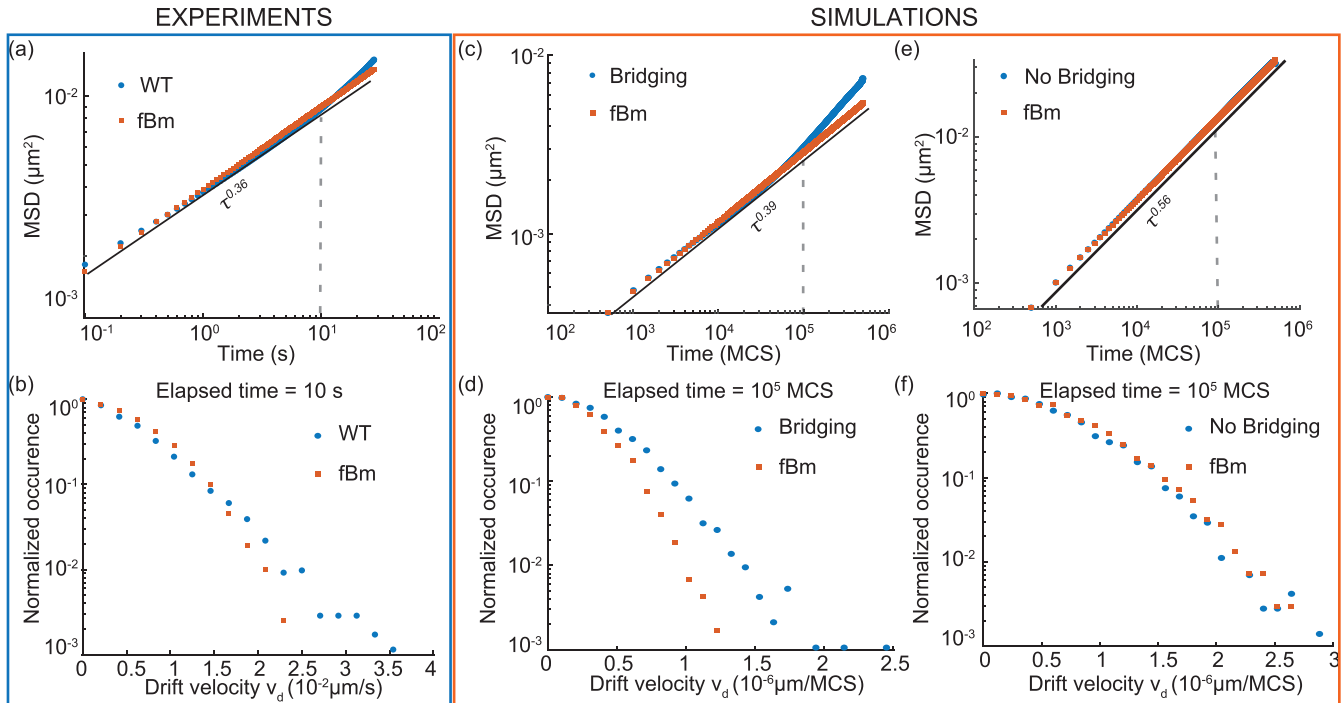| | Scaling exponent α | | | | | | | | | | | |
Strain	Set 1	Tracks	Set 2	Tracks	Set 3	Tracks	Set 4	Tracks	Set 5	Tracks	Set 6	Tracks	All
WT	0.31	3952	0.319	525	0.328	1193	0.339	477	0.3325	506			0.321 ± 0.011
ΔH-NS	0.364	12121	0.357	827	0.417	1647	0.407	1682	0.378	1062	0.364	750	0.380 ± 0.024

FIG. 4. (a) Ensemble-averaged MSD from WT cells (blue circles) is fit to an fBm model (orange squares, Fit $0.0008\tau^{0.36}$ μm^2, 6717 tracks). (b) Drift velocity of wild type tracks (blue circles) have a wider tail than from simulations of the parameter-matched fBm (orange squares). (c) Ensemble-averaged MSD from polymer simulations to an fBm model (orange squares, $\mu = 80$, $\lambda = 10^5$ MCS, Fit $0.0009\tau^{0.39}$ μm^2, 5200 tracks). (d) Drift velocity distribution from bridging simulations (blue circles) has a similar broad tail compared to the parameter-matched fBm model (orange square). (e) Same as (a), (c) but for polymers simulations without bridging. (f) The distributions of v_d overlap.

(Appendix D). We conclude that the bridging of chromosomal DNA by nucleoid associated proteins affects the nature of chromosome dynamics and can explain why the scaling exponent of chromosomal loci is more subdiffusive than expected from polymer dynamics alone.

IV. BRIDGING REPRODUCES RAPID CHROMOSOMAL MOVEMENTS

A previous analysis of chromosomal loci dynamics identified a subpopulation of fast moving trajectories that could not be explained by the null phenomenological model of fractional Brownian motion (fBm) [10]. Instead, these outliers, termed Rapid chromosomal movements (RCMs), were speculated to be due to an active machinery or some stress-relaxation mechanism [10,46]. They were identified by fitting the ensemble-averaged MSD curve to an fBm model [47] and then comparing the measured drift velocity distribution to that obtained by simulating the model. Here, the drift velocity v_d of a track is defined as the magnitude of the displacement along the major axis divided by the elapsed time [10]. Repeating this procedure, we found that our measurements displayed the same broad tail compared to the fBm simulations as in Javer *et al.* [Figs. 4(a) and 4(b)]. This was not dependent on the precise elapsed time used, nor on the deviation of the MSD curve from a perfect power law (or the range over which the parameter fitting was performed). Indeed, we found that RCMs were also present in the ∆H-NS strain, which displays a near perfect power law behavior [Figs. 5(a) and 5(b)].

Surprisingly, we found that our bridging simulations produced trajectories with a similar over-representation of high drift velocities compared to the fBm model [Figs. 4(c) and 4(d)] and this was directly attributable to the effect of bridging [Figs. 4(e) and 4(f)] and irrespective of the precise fitting and the elapsed time used [Figs. 4 and 5, Appendix C]. Note that, while bridging produces these outlier movements, overall it slows the dynamics of the polymer and therefore results in lower drift velocities. Consistent with this, the MSD and drift velocities of ∆H-NS were slightly greater than WT [Figs. 3(d) and 5(c)].

We explain the presence of RCMs in our simulations as follows. On timescales much longer than the mean bridge lifetime, each segment of the polymer is likely to be bridged for the same percentage of time and the dynamics are therefore relatively homogeneous. However, on timescales less than the bridge lifetime, there is greater heterogeneity—some segments will remain bridged throughout, others will remain unbridged. This heterogeneity cannot be captured by the single-population fBm model. Consistent with this, the disparity in the distributions increases as the drift velocity is measured over shorter elapsed times [Figs. 4(d) and 5(d)].

While we have not been able to quantitatively fit our simulations to the experimental data due to the increasingly computationally challenge of simulating longer bridge lifetimes and obtaining accurate statistics of the RCMs, we nevertheless conclude that bridging by NAPs provides a potential explanation for both the sub-diffusive scaling of chromosomal loci and the observed rare rapid chromosomal movements.
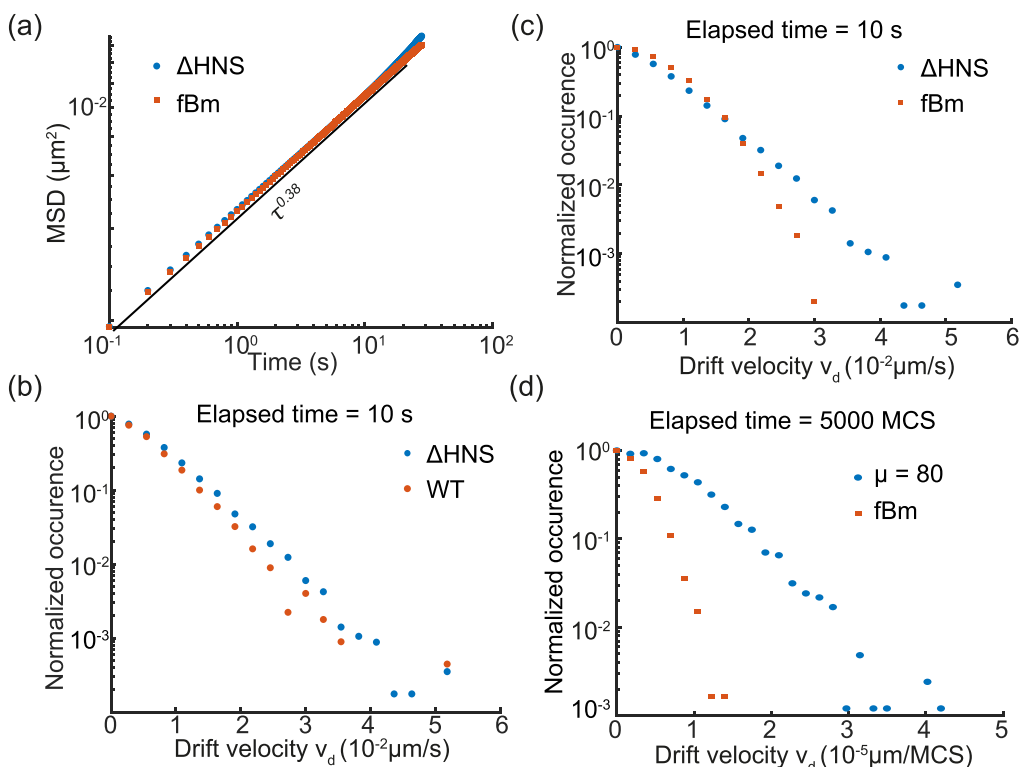
FIG. 5. (a) Ensemble averaged MSD from FBM simulations overlaid with ΔH-NS data (Fit, $0.0009\tau^{0.38}$). (b) Drift velocity distributions v_d from FBM simulations have a smaller tail than ΔH-NS data. (c) ΔH-NS has a slightly higher number, faster tracks than the wild type. (d) Drift velocity distribution comparisons as in Figs. 2(b) and 2(c), but at shorter elasped time of 5000 MCS the differences between bridging simulations and fBm model is amplified. The elasped time here is much shorter than the bridge lifetime leading to more heterogeneous populations than in Fig. 2(d). Parameters: $\mu = 80$, $\lambda = 10^5$ MCS.

V. TRANSITION TO A HIGHER EXPONENT PLACES BOUNDS ON BRIDGE LIFETIME

In our simulations, we observed that the MSD curve transitions at longer time lags to the exponent expected in the absence of bridging [Fig. 6(a)]. Interestingly, we found a similar upward transition in the experimental MSD curve of *ori* [Fig. 3(d)]. This was also observed in previous studies performed at the same (0.1 s) and longer time resolutions (1 s) and was associated to the RCMs discussed above [5,6,10]. While the cause of this transition is unknown and confounding

effects cannot be completely discounted, it is most apparent for the terminus (*ter*) region [5,6,10], which is affected by NAPs (MukBEF in particular) differently than the rest of chromosome [14]. In our simulations, the transition is due to bridging not affecting the exponent on timescales longer than the bridge lifetime. Indeed, we observe a linear relationship between the transition location and the bridge lifetime λ [Fig. 6(b)]. We also note that the transition was not visible in the MSD curve of ΔH-NS strain (at least within the measured range) [Fig. 5(a)], which could be explained by this strain having a longer average bridge lifetime.
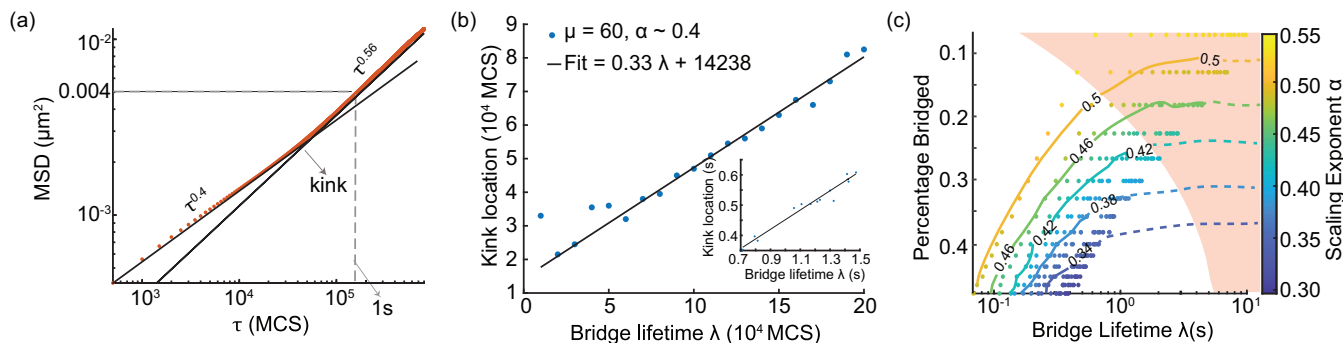

FIG. 6. (a) MSD curve transitions to a higher exponent $\alpha \sim 0.56$. (b) Location of the kink depends linearly on the bridge lifetime (λ). Inset shows the same plot after conversion to seconds. (c) Phase diagram from Fig. 1(c) converted to seconds. The contours of α are overlaid. Dashed lines are estimated projections to higher values of λ. Shading indicates that the kink lies beyond 1 s.
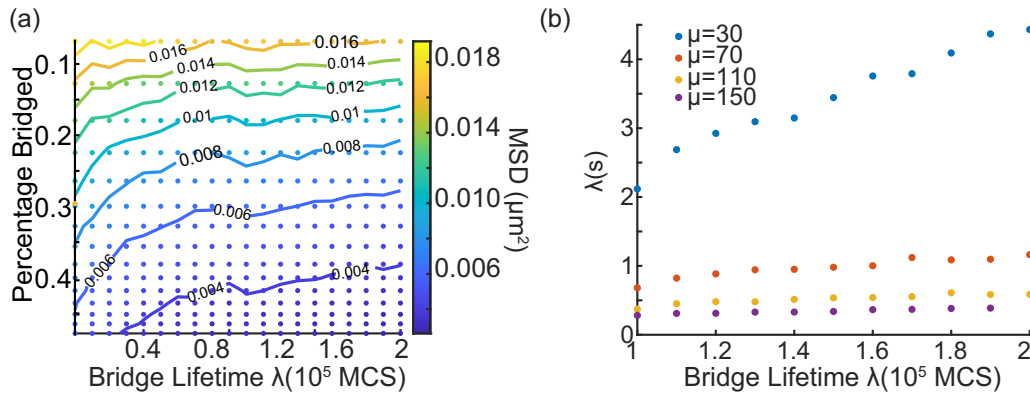
FIG. 7. (a) Phase diagram of MSD at 25000 MCS for different parameters. MSD value reached at longer time delays decreases with increasing bridging. (b) Conversion between bridge lifetime λ in MCS to seconds. $\lambda(s)$ increases linearly with λ (MCS) but the slope decreases sharply for higher levels of bridging. Hence, it is computationally challenging to access longer bridge lifetimes in seconds for higher levels of bridging.

We next wondered whether the location of the transition could be used to infer a bound on the effective bridge lifetime. In this direction, we set the internal timescale of our simulations by matching the MSD of *ori* at a lag of 1 s [Fig. 3(d)]. With our lattice spacing of $0.0056\,\mu m$ (chosen to have sufficient spatial resolution at this displacement), this MSD value was reached at a lag of $\approx 10^5$ MCS [Fig. 6(a)]. We can then convert our simulation results to seconds by assigning 10^5 MCS ≈ 1 s. Doing this for all points in the phase diagram we obtain a relationship between the equilibrium percentage of monomers bridged and the bridge lifetime λ in seconds for different values of the scaling exponent [Fig. 6(c)]. We have extended the contours of fixed exponent to longer lifetimes by hand as it becomes increasingly computationally challenging to access longer bridge lifetimes (in seconds), especially for the lowest exponents, due to the slow dynamics of the polymer (each second corresponds to an increasingly large number of MCS) [Figs. 7(a) and 7(b)]. While the scaling exponent can be measured experimentally, the degree of bridging and the effective bridge lifetime are more challenging to quantify. Nevertheless, the relationship between these variables that we have uncovered here should be useful in interpreting future experimental results and contributes to our understanding of chromosome dynamics.

We next use the linear relationship of the kink location to the bridge lifetime [Fig. 6(b)] to estimate the location of the transition in seconds at each point in the phase diagram. In particular, we identify the region of the phase diagram in which the transition occurs beyond a delay of 1 s, as seen in our data and other measurements. For the exponent we observe, $\alpha \sim 0.32$, we find a lower bound on the effective bridge lifetime of around 5 s, a reasonable estimate given the relative slow dynamics of chromosomal loci. While measurements of bridge lifetimes of the various NAPs are lacking, estimates for H-NS and HU can be taken from the timescale of their recovery after photobleaching (FRAP) which have given 50 s [48] and 1 s [49], respectively.

VI. DISCUSSION

Our results provide insight into the role of DNA bridging in determining chromosome loci dynamics within bacterial cells.

We have shown that bridging, at physically plausible levels and lifetimes, can explain the subdiffusive scaling exponent of bacterial chromosomal loci. Consistent with this, a strain deleted of the DNA bridging protein H-NS exhibited an increased scaling exponent. Our model also displays a similar upturn in the ensemble-averaged MSD curve as observed experimentally and we used this to obtain a lower bound on the effective bridge lifetime at the *ori* locus of about 5 s.

Bridging can also qualitatively reproduce the rare but ubiquitous rapid chromosomal movements (RCMs) that are observed within experimental trajectories, in contrast to the null phenomenological model of fractional Brownian motion. The RCMs in our model are due to the heterogeneity in the bridging state of a locus on timescales smaller than or comparable to the bridge lifetime. This is in contrast to a previous proposal that RCMs necessarily arise due to an active stress release mechanism [10,50]. Furthermore, bridging is consistent with recent work showing that cell compression lowers the exponent of chromosomal loci but not that of diffusive particles [6]. A lower cell volume increases the density of DNA and therefore increases the rate of bridge formation, lowering the exponent. More broadly, by characterizing the relationship between an equilibrium quantity, the number of bridges, and a dynamic quantity, the mean bridge lifetime (λ), our framework provides an intuitive parameter landscape for bacterial chromosome dynamics that will help guide future studies.

APPENDIX A: SIMULATION DETAILS

Each simulation is started from a random conformation of the polymer. Monomer diffusion and bridging is implemented in the following manner.

(1) Select a monomer at random and attempt a diffusive move (BFM algorithm).
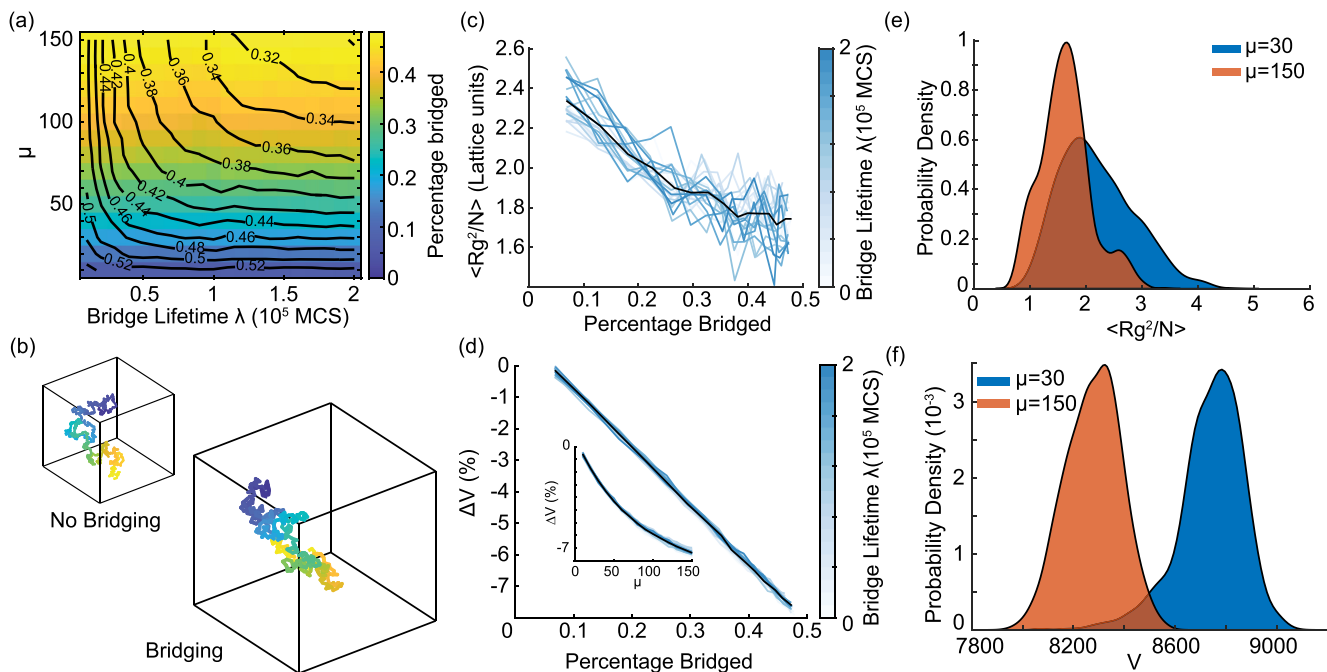
FIG. 8. (a) Phase diagram of the dynamic bridging model in the $\mu = p\lambda$ and λ space. Note that μ is positively related to the percentage of monomers bridged. Contours indicate a fixed exponent α. (b) Example polymer conformations with and without bridging. (c) Radius of Gyration $\langle R_g^2/N \rangle$ as function of Percentage Bridged. (d) The change in excluded volume relative to the nonbridging polymer ΔV decreases linearly with bridging. (Inset) The relationship between ΔV and the model parameter μ. Black line indicates the average across bridge lifetimes. (e) Distributions of $\langle R_g^2/N \rangle$ are overlapping for different levels of bridging. (f) Distributions of V_{occupied} are significantly separated.

(2) Select a random monomer and if colocalized with another free monomer (distance < 3 lattice units), attempt a bridge with probability p.

(3) Select a random monomer and if bridged, remove the bridge with probability $\frac{1}{\lambda}$.

(4) Repeat.

A set of N moves is defined as a single MCS and we sample the configuration every 500 MCS. Note that a bridged monomer can still diffuse as long as the bridge partner is less than three lattice units away. We start the Monte Carlo sampling after 5λ MCS to ensure sufficient equilibration of the polymer.

The phase diagram is calculated as an average from multiple simulations for each parameter value $\mu = p\lambda$, λ. From our simulations, we calculate the ensemble averaged MSD at lag τ defined by

$$\langle r^2(\tau) \rangle = \frac{1}{N} \frac{1}{T-\tau} \sum_{n=1}^{N} \sum_{t=1}^{T-\tau} [\mathbf{r}_n(t+\tau) - \mathbf{r}_n(t)]^2. \quad \text{(A1)}$$

We perform a linear fit to the logarithm of the MSD curves

$$\log(\langle r^2(\tau) \rangle) = \alpha \log(\tau) + D_{\text{app}} \quad \text{(A2)}$$

up to a delay of 20 000 MCS and obtain ensemble averaged α. The data in Figs. 8(d) and 1(c) are obtained from 50 ($\lambda \leqslant 10^5$) and 30 ($\lambda > 10^5$) independent simulations for each parameter. The ensemble averaged MSD curves are calculated from tracks of every 20th monomer on the polymer (600–1000 tracks per parameter).

APPENDIX B: EQUILIBRIUM PROPERTIES

We found that bridging, unsurprisingly, results in compaction of the polymer [Fig. 8(b)], as seen in previous studies [33]. This could be quantified using the radius of gyration [Fig. 8(c)]

$$\langle R_g^2 \rangle \equiv \frac{1}{N} \sum_{i=1}^{N} (\mathbf{r}_i - \mathbf{r}_{cm})^2. \quad \text{(B1)}$$

However, we found it to be a relatively noisy measure of polymer size. We therefore also examined the excluded volume of the polymer (V), defined in the previous section. Excluded volume V shows a clear linear decrease with the number of bridges formed [Fig. 8(d)]. Excluded volume was found to be a more robust measure in that different parameter values could be more easily distinguished [Figs. 8(e) and 8(f)]. This was independent of the bridge lifetime λ with curves of different λ collapsing onto the same line. The latter confirms results from previous Brownian dynamics simulations that the polymer relaxation time can be controlled (through the bridge lifetime) independently of the equilibrium structure [51].

1. Mesh size decreases in the presence of bridging

Another measure of compaction is the mesh size. While it is challenging to measure accurately in simulations, it has been recently estimated for the *E. coli* nucleoid to be around 50 nm [54]. To estimate the mesh size ξ in our simulations we first determine the probability of finding a monomer at a distance r and $r + dr$ from another randomly chosen monomer. This is given by $4\pi\rho r^2 g(r)\, dr$, where $\rho = 0.01$ is the density
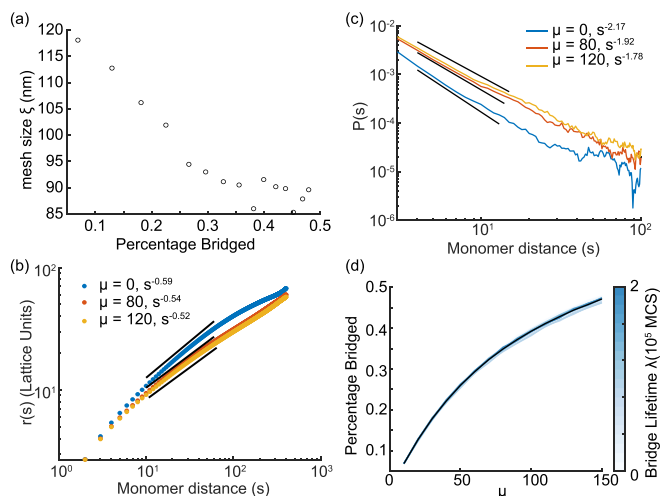
FIG. 9. (a) Mesh size (ξ) decreases with increasing bridges. (b) End to end distance for subsegments on the chain scale as $\langle R \rangle \sim s^\nu$. We observe an exponent $\nu = 0.59$ in the absence of bridging as expected for a self-avoiding polymer. The scaling exponent decreases with increasing bridging. But, we do not observe a plateauing of the curves which is indicative of the globule state. (c) The contact probability $P(s)$ between monomers is plotted as function of monomer distance (s). In the absence of bridging (blue curve), we find $P(s) \sim s^{2.18}$ as expected for a self-avoiding chain in a good solvent [52,53]. With increasing bridging the exponent increases, but for our level of bridging we are never below the compact globule regime. $\lambda = 100\,000$ MCS in (b), (c). (d) Percentage of monomers bridged increases with μ and is independent of bridge lifetime.

of the polymer and $g(r)$ is a radial density function. For a semi dilute polymer with $r \gg \xi_c$, $g(r)$ is expected to have the form

$$g(r) = 1 + \frac{A}{r} exp(-r/\xi_c), \qquad \text{(B2)}$$

where $A > 0$ and $\xi_c > 0$. ξ_c is the correlation length of the polymer which is approximately the same as the mesh size ξ for a semidilute polymer [55]. We calculate $g(r)$ from our simulations and fit to (B2), and find the mesh size (ξ) for different parameters. We find that mesh size decreases with increased bridging and has a range of values between 120–85 nm [Fig. 9(a)] for the system parameters used. As we will see below, the disparity with the experimental value may be because our simulated system is less confined that *E. coli* nucleoid.

2. End-to-End scaling and contact probability

The end-to-end distance for subsegments on the chain scale as $r(s) \sim s^\nu$ with $\nu \approx 0.588$ [2] for a free polymer [Fig. 9(b)]. We observe that with increasing bridging the exponent decreases, but stays above the transition value of $\nu = 0.5$. Similar behavior was observed for the contact probability [Fig. 9(c)]. Thus, for the parameters studied the polymer does not enter the globular regime, which has been studied elsewhere [30,33,51]. Note that like $\langle R_g^2 \rangle$, the aforementioned equilibrium quantities do not depend on the bridge lifetime.
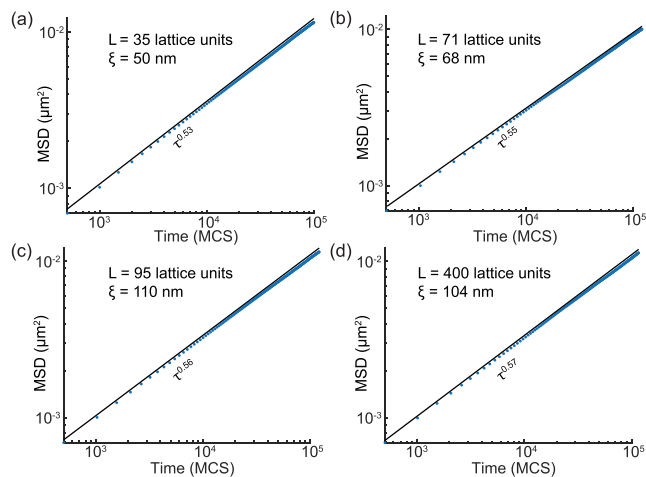

FIG. 10. (a)–(d) Confinement affects the scaling exponent of MSD even in the absence of bridging. Mesh size decreases with increasing confinement. Parameters: lattice size L, mesh size ξ, polymer length N = 400.

3. Matching chromosome density versus confinement

Thus far, our simulation parameters were chosen to match the density of DNA within an *E. coli* cell rather than the effect of confinement due to the cell boundaries (measured as the unconfined Rg of the polymer relative to the dimension of the box $\frac{2Rg}{L}$) since the former quantity is likely to more strongly affect the probability of bridge formation. The density d scales linearly with number of monomers N, while confinement scales as $R_g \sim N^\nu$, where $\nu = 0.588$ making it impossible to match both quantities at the same time. Nevertheless, since the *E. coli* chromosome is confined within the cell (filling the cytosol and expanding with cell growth [7]), we also briefly examined the effect of confinement. The results on the scaling exponent were qualitatively the same as shown in the main text but with a lower value for the same set of parameters μ, λ due to the higher number of bridges. This is consistent with recent work showing that cell compression lowers the MSD scaling exponent of chromosomal loci but not that of diffusive particles [6]. It also motivates our use in the main text of the fraction of monomers bridged instead of the parameters μ.

Additionally, we found that confinement could reduce the mesh size even without bridging to the experimentally measured value of 50 nm [Fig. 10(a)] [54]. Note also that as confinement increases, α decreases toward $\alpha \approx 0.5$, i.e., confinement screens the effect of self-avoidance (Fig. 10) [37].

4. Circular polymer in cuboidal geometry

To briefly examine the effected of a confined geometry, we simulate a circular polymer of length $N = 440$ monomers in a cuboidal box with dimensions $L_x = 88$, $L_y = 22$, and $L_z = 22$ matching the 4:1 aspect ratio of *E. coli* cells (Fig. 11) and given a system density as in Fig. 10(a). We then measured the monomer density across 1000 independent configurations. In the case of the polymer with no bridges, we observed a
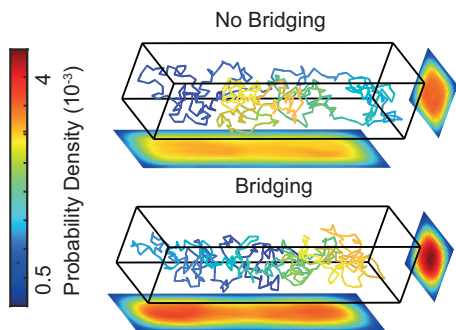
FIG. 11. A circular polymer in a cuboid with hard walls matching the confinement of *E. coli* cells. In the presence of bridging, the polymer is compacted and has a density that decreases across the cross section. Lattice dimensions $88 \times 22 \times 22$.

uniform distribution. In contrast, the bridging polymer shows a radially decreasing density across the cross section. This is notable, as direct imaging of an abundant NAP HU in *E. coli* also revealed a similar decreasing radial density of the chromosome across the cross-section of the cell [56,57].

APPENDIX C: BRIDGING EXPLAINS SUBPOPULATIONS

Previously, Javer *et al.* [10] compared the distribution of track drift velocities, defined as the magnitude of the

displacement along the major axis between two time points divided by the elapsed time, with that obtained by a fractional Brownian motion (fBm) model, parameter-matched to the ensemble-averaged MSD curve. They noticed that a subpopulation of tracks with a drift velocity greater than that expected for the fBm model as we discuss in Fig. 4 of the main text. They also found this population displayed a qualitatively different ensemble averaged MSD curve (a higher exponent at longer time lags) compared to the rest of the population.

For comparison, we performed the same analysis on our data and selected the subset of outlier trajectories (39 of 6717) with drift velocity $v_d > 0.012$ μm s^{-1} [Fig. 12(a)]. We found that the ensemble averaged MSD curves indeed show a transition to faster dynamics at longer timescales [see Fig. 12(b)], as in [10]. This was also the case for our bridging simulations [Fig. 12(c)]. The tracks with higher v_d have a higher (generalized) diffusion coefficient than the majority population and transition to a higher exponent at long time lags [Fig. 12(d)]. However, caution is warranted interpreting this analysis since we are self-selecting a "fast" subpopulation. Nevertheless, repeating the procedure for simulated fBm trajectories (and taking the fastest 0.5%), gave MSD curves that overlap at short time lags and only deviate at long time lags [Fig. 12(e)], i.e., the populations have the same (generalized) diffusion coefficient. This provides further support for our conclusion that bridging, in contrast to fBm, can reproduce the observed loci dynamics.
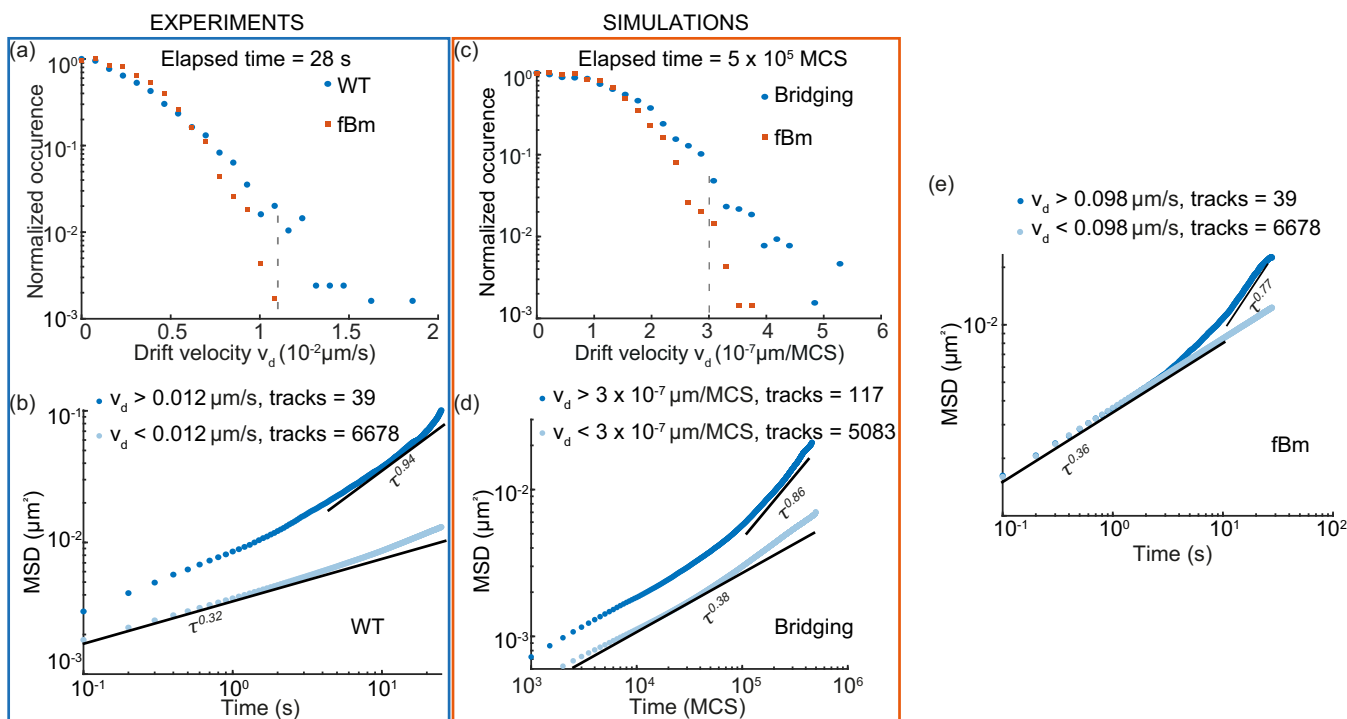

FIG. 12. (a) Drift velocity distribution comparisons between WT data and fBm measured over 28s (entire track length). (b) Ensemble averaged MSD of the wild type strain with tracks selected based on drift velocity v_d (grey dashed line in (a) shows the v_d threshold). Tracks with v_d greater that fBm distribution display different dynamics to the rest of the population and transition to a higher exponent at longer time lags. (c) Same as in (a) for the bridging simulations with v_d defined over the entire track length of 5×10^5 MCS. (d) We find a similar subset of tracks (split based v_d, grey dashed line in (c)) which transition to higher exponent at longer time lags. Parameters $\mu = 80$, $\lambda = 10^5$ MCS. (e) We select the indicated sub-population of faster moving tracks in the fBm simulations. The ensemble-averaged MSD of the faster tracks deviate from the rest of the tracks only at longer time lags and do not reproduce the behavior seen in the experimental data in (b).
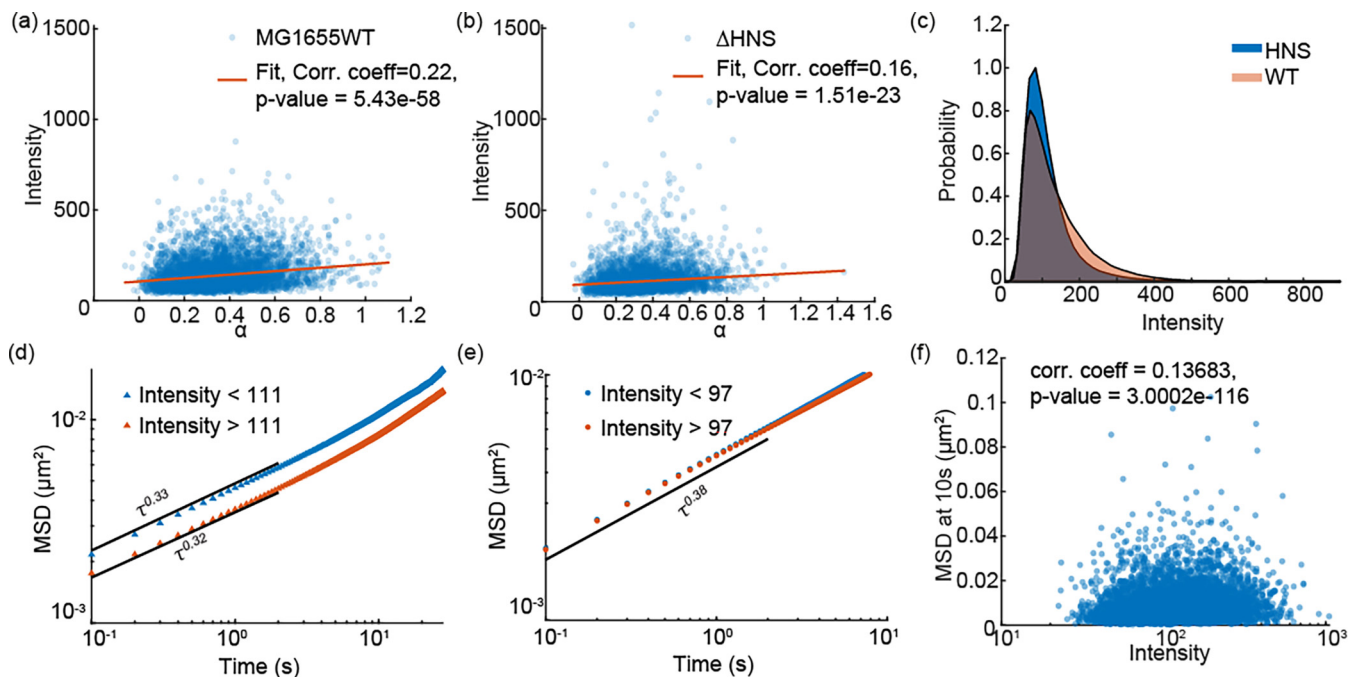
FIG. 13. (a) Mean intensity of WT tracks plotted versus scaling exponent α fitted to the entire track length. Shows weak positive correlation. (b) Same as in (a) but for the mutant ΔH-NS. (c) Intensity distributions of WT and ΔH-NS is plotted. WT distribution has a broader tail. (d) Ensemble averaged MSD of WT plotted for two different subpopulations with intensity $I > \mathrm{median}(I)$ and $I < \mathrm{median}(I)$. Scaling exponent α shows marginal change while D_{app} decreases with higher intensities [5]. (e) Same as in (d) but for the mutant. The subpopulations overlap. (f) Intensity of loci in the WT at a MSD of 10 s. We find a very weak positive correlation.

APPENDIX D: INTENSITY OF SPOTS DOES NOT EXPLAIN DIFFERENCES IN SCALING EXPONENTS

We wondered if the difference in MSD scaling exponents between the WT and mutant could be related to the intensity, as it was previously shown that the mobility of loci depends inversely on their intensity [5]. In our experimental data, we find that the WT and mutant have comparable intensity distributions and show a very weak correlation between the loci intensity and the scaling exponent α [Figs. 13(a) and 13(b)]. We also found that the intensity distributions of the strains was comparable, while the WT had a slightly fatter tail [Fig. 13(c)]. Comparing the ensemble-averaged MSD of tracks with lower and higher intensity, we found that while intensity affects the apparent diffusion constant D_{app}, it has a marginal effect on the scaling exponent α [Figs. 13(d) and 13(e)]. The intensity of loci also shows a very weak correlation with the MSD at 10 s [Fig. 13(f)]. Hence, we conclude that the intensity of loci does not explain the differences between the ensemble-averaged MSD exponents of WT and ΔH-NS.

APPENDIX E: VARIABILITY IN α AND TRANSITION IN MSD CURVE

Time Averaged MSD of a single particle suffers from high variation and random errors. A possible way to mitigate this is by studying the ensemble averaged MSD. While this is generally adequate for estimating various diffusion parameters, it has been argued that it suffers from inaccuracies if the underlying population has heterogeneous subdiffusion. We can calculate the mean logarithmic squared displacement (MLSD)

to account for the exponential dependence on delays [58]

$$r_l^2(\tau) = \log\left(\sum_{t=1}^{T-\tau} [r_n(t+\tau) - r_n(\tau)]^2\right). \quad (E1)$$

We have an effective exponent μ,

$$\langle r_l^2(\tau) \rangle = \langle \log(D) \rangle + \mu \log(\tau). \quad (E2)$$

Analyzing our experimental trajectories of WT *E. coli* cells, this procedure did not produce any significant differences in our MSD curves [Fig. 14]. While it does not exclude other effects like photobleaching, the underlying heterogeneity in α at different time lags might be a real effect arising from a subpopulation of trajectories with more mobility (RCMs).
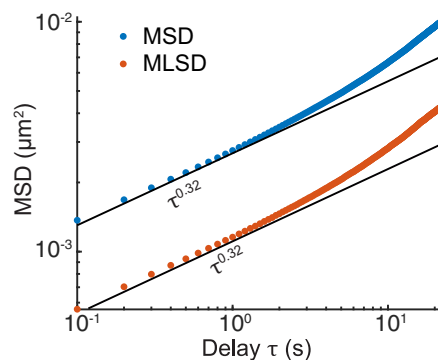

FIG. 14. Mean logarithmic squared displacement (MLSD) also shows a transition to higher exponent at longer delays.

[1] I. Teraoka, *Polymer Solutions: An Introduction to Physical Properties* (Wiley, New York, 2004).

[2] M. Doi, P. Doi, and S. Edwards, *The Theory of Polymer Dynamics*, International Series of Monographs on Physics (Clarendon Press, Oxford, 1986).

[3] S. C. Weber, A. J. Spakowitz, and J. A. Theriot, Bacterial Chromosomal Loci Move Subdiffusively through a Viscoelastic Cytoplasm, Phys. Rev. Lett. **104**, 238102 (2010).

[4] S. C. Weber, A. J. Spakowitz, and J. A. Theriot, Nonthermal ATP-dependent fluctuations contribute to the in vivo motion of chromosomal loci, Proc. Natl. Acad. Sci. **109**, 7338 (2012).

[5] A. Javer, Z. Long, E. Nugent, M. Grisi, K. Siriwatwetchakul, K. D. Dorfman, P. Cicuta, and M. Cosentino Lagomarsino, Short-time movement of *E. coli* chromosomal loci depends on coordinate and subcellular localization, Nat. Commun. **4**, 3003 (2013).

[6] S. Yu, J. Sheats, P. Cicuta, B. Sclavi, M. Cosentino Lagomarsino, and K. D. Dorfman, Subdiffusion of loci and cytoplasmic particles are different in compressed Escherichia coli cells, Communications Biology **1** (2018).

[7] F. Wu, P. Swain, L. Kuijpers, X. Zheng, K. Felter, M. Guurink, J. Solari, S. Jun, T. S. Shimizu, D. Chaudhuri, B. Mulder, and C. Dekker, Cell boundary confinement sets the size and position of the *E. coli* chromosome, Curr. Biol. **29**, 2131 (2019).

[8] E. Crozat, C. Tardin, M. Salhi, P. Rousseau, A. Lablaine, T. Bertoni, D. Holcman, B. Sclavi, P. Cicuta, and F. Cornet, Post-replicative pairing of sister ter regions in Escherichia coli involves multiple activities of MatP, Nat. Commun. **11**, 3796 (2020).

[9] S. C. Weber, J. A. Theriot, and A. J. Spakowitz, Subdiffusive motion of a polymer composed of subdiffusive monomers, Phys. Rev. E **82**, 011913 (2010).

[10] A. Javer, N. J. Kuwada, Z. Long, V. G. Benza, K. D. Dorfman, P. A. Wiggins, P. Cicuta, and M. C. Lagomarsino, Persistent super-diffusive motion of Escherichia coli chromosomal loci, Nat. Commun. **5**, 3854 (2014).

[11] J. Stavans and A. Oppenheim, DNA–protein interactions and bacterial chromosome architecture, Physical Biology **3**, R1 (2006).

[12] R. T. Dame and M. Tark-Dame, Bacterial chromatin: Converging views at different scales, Curr. Opin. Cell Biol. **40**, 60 (2016).

[13] R. T. Dame, F. Z. M. Rashid, and D. C. Grainger, Chromosome organization in bacteria: mechanistic insights into genome structure and function, Nat. Rev. Genet. **21**, 227 (2020).

[14] V. S. Lioy, A. Cournac, M. Marbouty, S. Duigou, J. Mozziconacci, O. Espéli, F. Boccard, and R. Koszul, Multiscale structuring of the *E. coli* chromosome by nucleoid-associated and condensin proteins, Cell **172**, 771 (2018).

[15] J. J. Messelink, M. C. van Teeseling, J. Janssen, M. Thanbichler, and C. P. Broedersz, Learning the distribution of single-cell chromosome conformations in bacteria reveals emergent order across genomic scales, Nat. Commun. **12**, 1963 (2021).

[16] T. Agarwal, G. P. Manjunath, F. Habib, and A. Chatterji, Bacterial chromosome organization. II. Few special cross-links, cell confinement, and molecular crowders play the pivotal roles, J. Chem. Phys. **150**, 144909 (2019).

[17] A. Wasim, A. Gupta, and J. Mondal, A Hi-C data-integrated model elucidates *E. coli* chromosome's multiscale

[18] P. Bera, A. Wasim, and J. Mondal, Hi-c embedded polymer model of escherichia coli reveals the origin of heterogeneous subdiffusion in chromosomal loci, Phys. Rev. E **105**, 064402 (2022).

[19] O. Shukron, V. Piras, D. Noordermeer, and D. Holcman, Statistics of chromatin organization during cell differentiation revealed by heterogeneous cross-linked polymers, Nat. Commun. **10**, 2626 (2019).

[20] R. Takaki, A. Dey, G. Shi, and D. Thirumalai, Theory and simulations of condensin mediated loop extrusion in dna, Nat. Commun. **12**, 5865 (2021).

[21] L. Leibler, M. Rubinstein, and R. H. Colby, Dynamics of reversible networks, Macromolecules **24**, 4701 (1991).

[22] M. Rubinstein and A. N. Semenov, Thermoreversible gelation in solutions of associating polymers. 2. Linear dynamics, Macromolecules **31**, 1386 (1998).

[23] M. Rubinstein and A. V. Dobrynin, Associations leading to formation of reversible networks and gels, Curr. Opin. Colloid Interface Sci. **4**, 83 (1999).

[24] M. Rubinstein and A. N. Semenov, Dynamics of entangled solutions of associating polymers, Macromolecules **34**, 1058 (2001).

[25] M. Nicodemi and A. Prisco, Thermodynamic pathways to genome spatial organization in the cell nucleus, Biophys. J. **96**, 2168 (2009).

[26] M. Tark-Dame, H. Jerabek, E. M. Manders, D. W. Heermann, and R. van Driel, Depletion of the chromatin looping proteins ctcf and cohesin causes chromatin compaction: Insight into chromatin folding by polymer modelling, PLoS Comput. Biol. **10**, e1003877 (2014).

[27] J. Mateos-Langerak, M. Bohn, W. De Leeuw, O. Giromus, E. M. Manders, P. J. Verschure, M. H. Indemans, H. J. Gierman, D. W. Heermann, R. Van Driel, and S. Goetze, Spatially confined folding of chromatin in the interphase nucleus, Proc. Natl. Acad. Sci. USA **106**, 3812 (2009).

[28] M. Barbieri, M. Chotalia, J. Fraser, L.-M. Lavitas, J. Dostie, A. Pombo, and M. Nicodemi, Complexity of chromatin folding is captured by the strings and binders switch model, Proc. Natl. Acad. Sci. **109**, 16173 (2012).

[29] A. M. Chiariello, C. Annunziatella, S. Bianco, A. Esposito, and M. Nicodemi, Polymer physics of chromosome large-scale 3D organisation, Sci. Rep. **6**, 29775 (2016).

[30] M. Nicodemi and A. Pombo, Models of chromosome structure, Curr. Opin. Cell Biol. **28**, 90 (2014).

[31] A. Hofmann and D. W. Heermann, The role of loops on the order of eukaryotes and prokaryotes, FEBS Lett. **589**, 2958 (2015).

[32] C. A. Brackley, S. Taylor, A. Papantonis, P. R. Cook, and D. Marenduzzo, Nonspecific bridging-induced attraction drives clustering of dna-binding proteins and genome organization, Proc. Natl. Acad. Sci. **110**, E3605 (2013).

[33] M. Bohn and D. W. Heermann, Diffusion-driven looping provides a consistent framework for chromatin organization, PLoS ONE **5**, e12218 (2010).

[34] I. Carmesin and K. Kremer, The bond fluctuation method: a new effective algorithm for the dynamics of polymers in all spatial dimensions, Macromolecules **21**, 2819 (1988).

[35] H. P. Deutsch and K. Binder, Interdiffusion and selfdiffusion in polymer mixtures: A Monte Carlo study, J. Chem. Phys. **94**, 2294 (1991).

[36] M. Wengenmayr, R. Dockhorn, T. Müller, H. Rabbel, C. Jentzsch, and M. Werner, Lemonade-project/lemonade: Lemonade v2.2.1, Zenodo (2020).

[37] S. C. Weber, M. A. Thompson, W. E. Moerner, A. J. Spakowitz, and J. A. Theriot, Analytical tools to distinguish the effects of localization error, confinement, and medium elasticity on the velocity autocorrelation function, Biophys. J. **102**, 2443 (2012).

[38] K. E. Polovnikov, M. Gherardi, M. Cosentino-Lagomarsino, and M. V. Tamm, Fractal Folding and Medium Viscoelasticity Contribute Jointly to Chromosome Dynamics, Phys. Rev. Lett. **120**, 088101 (2018).

[39] Y. Li, K. Sergueev, and S. Austin, The segregation of the Escherichia coli origin and terminus of replication, Mol. Microbiol. **46**, 985 (2002).

[40] R. Mercier, M. A. Petit, S. Schbath, S. Robin, M. El Karoui, F. Boccard, and O. Espéli, The MatP/matS site-specific system organizes the terminus region of the *E. coli* chromosome into a macrodomain, Cell **135**, 475 (2008).

[41] H. J. Nielsen, Y. Li, B. Youngren, F. G. Hansen, and S. Austin, Progressive segregation of the Escherichia coli chromosome, Mol. Microbiol. **61**, 383 (2006).

[42] H. J. Nielsen, J. R. Ottesen, B. Youngren, S. J. Austin, and F. G. Hansen, The Escherichia coli chromosome is organized with the left and right chromosome arms in separate cell halves, Mol. Microbiol. **62**, 331 (2006).

[43] O. Espeli, R. Mercier, and F. Boccard, DNA dynamics vary according to macrodomain topography in the *E. coli* chromosome, Mol. Microbiol. **68**, 1418 (2008).

[44] M. Stouf, J. C. Meile, and F. Cornet, FtsK actively segregates sister chromosomes in Escherichia coli, Proc. Natl. Acad. Sci. USA **110**, 11157 (2013).

[45] https://github.com/ver228/bacteria-loci-tracker.

[46] M. Gherardi, L. Calabrese, M. Tamm, and M. Cosentino Lagomarsino, Model of chromosomal loci dynamics in bacteria as fractional diffusion with intermittent transport, Phys. Rev. E **96**, 042402 (2017).

[47] W. Deng and E. Barkai, Ergodic properties of fractional brownian-langevin motion, Phys. Rev. E **79**, 011112 (2009).

[48] M. Kumar, M. S. Mommer, and V. Sourjik, Mobility of cytoplasmic, membrane, and DNA-binding proteins in Escherichia coli, Biophys. J. **98**, 552 (2010).

[49] K. Floc'h, F. Lacroix, P. Servant, Y. S. Wong, J. P. Kleman, D. Bourgeois, and J. Timmins, Cell morphology and nucleoid dynamics in dividing Deinococcus radiodurans, Nat. Commun. **10**, 1 (2019).

[50] M. C. Joshi, A. Bourniquel, J. Fisher, B. T. Ho, D. Magnan, N. Kleckner, and D. Bates, Escherichia coli sister chromosome separation includes an abrupt global transition with concomitant release of late-splitting intersister snaps, Proc. Natl. Acad. Sci. USA **108**, 2765 (2011).

[51] C. E. Sing and A. Alexander-Katz, Equilibrium structure and dynamics of self-associating single polymers, Macromolecules **44**, 6962 (2011).

[52] J. des Cloizeaux, Short range correlation between elements of a long polymer in a good solvent, J. Phys. France **41**, 223 (1980).

[53] S. Redner, Distribution functions in the interior of polymer chains, J. Phys. A: Math. Gen. **13**, 3525 (1980).

[54] Y. Xiang, I. V. Surovtsev, Y. Chang, S. K. Govers, B. R. Parry, J. Liu, and C. Jacobs-Wagner, Interconnecting solvent quality, transcription, and chromosome folding in Escherichia coli, Cell **184**, 3626 (2021).

[55] V. Sorichetti, V. Hugouvieux, and W. Kob, Determining the mesh size of polymer solutions via the pore size distribution, Macromolecules **53**, 2568 (2020).

[56] J. K. Fisher, A. Bourniquel, G. Witz, B. Weiner, M. Prentiss, and N. Kleckner, Four-dimensional imaging of *E. coli* nucleoid organization and dynamics in living cells, Cell **153**, 882 (2013).

[57] S. G. Remesh, S. C. Verma, J. H. Chen, A. A. Ekman, C. A. Larabell, S. Adhya, and M. Hammel, Nucleoid remodeling during environmental adaptation is regulated by HU-dependent DNA bundling, Nat. Commun. **11**, 2905 (2020).

[58] E. Kepten, I. Bronshtein, and Y. Garini, Improved estimation of anomalous diffusion exponents in single-particle tracking experiments, Phys. Rev. E **87**, 052713 (2013).